

Ion-beam-induced magnetic transformation of CO-stabilized fcc Fe films on Cu(100)

Sameena Shah Zaman, Hinnerk Oßmer, Jakub Jonner, Zbyněk Novotný, Andreas Buchsbaum, Michael Schmid, and Peter Varga

Institut für Angewandte Physik, Vienna University of Technology, 1040 Vienna, Austria

(Received 24 September 2010; published 1 December 2010)

We have grown 22-ML-thick Fe films on a Cu(100) single crystal. The films were stabilized in the face-centered-cubic (fcc) γ phase by adsorption of carbon monoxide during growth, preventing the transformation to the body-centered-cubic (bcc) α phase. A structural transformation of these films from fcc to bcc can be induced by Ar^+ ion irradiation. Scanning-tunneling microscopy images show the nucleation of bcc crystallites, which grow with increasing Ar^+ ion dose and eventually result in complete transformation of the film to bcc. Surface magneto-optic Kerr effect measurements confirm the transformation of the Fe film from paramagnetic (fcc) to ferromagnetic (bcc) with an in-plane easy axis. The transformation can also be observed by low-energy electron diffraction. We find only very few nucleation sites of the bcc phase and argue that nucleation of the bcc phase happens under special circumstances during resolidification of the molten iron in the thermal spike after ion impact. Intermixing with the Cu substrate impedes the transformation. We also demonstrate the transformation of films coated with Au to protect them from oxidation at ambient conditions.

DOI: [10.1103/PhysRevB.82.235401](https://doi.org/10.1103/PhysRevB.82.235401)

PACS number(s): 75.70.Ak, 68.55.-a, 75.50.Bb, 79.20.Rf

I. INTRODUCTION

As a bulk material, Fe exists in the α phase [body-centered-cubic (bcc); ferromagnetic] at room temperature (RT) and attains the γ phase [face-centered cubic (fcc); paramagnetic] only above 1180 K.^{1,2} The lattice constants of Cu, fcc Fe, and bcc Fe are 3.615, 3.57, and 2.866 Å, respectively. As the lattice mismatch between fcc Fe and Cu is small (<2%), pseudomorphic growth of metastable fcc Fe on Cu can be expected and was already observed in 1967 by Jesser and Matthews for Fe/Cu(100).³ Since then, it was found out that Fe on Cu(100) shows surprising magnetic⁴⁻²³ and structural properties^{11,12,19,24-38} depending on the Fe layer thickness¹³ and temperature,^{7,13,26,39} and it is still a subject of intensive research.

Early investigations show contradictory results for some aspects of this system, e.g., the critical thickness of the transformation from fcc to the bulklike bcc phase was reported to be 11 monolayer (ML) (Ref. 11) and 17 ML (Ref. 12); in hindsight, this issue should be probably attributed to different impurity levels.^{40,41} There was also confusion about the ground state of fcc Fe, which is usually antiferromagnetic,^{7,42} while some observations have pointed toward fcc Fe/Cu films with a ferromagnetic ground state especially at low thickness.^{6,9,43} This issue was resolved by Biedermann *et al.*^{2,35,44} using atomically resolved scanning tunneling microscopy, which pinpoints the bcc-like nature of these films as the true source of ferromagnetism. Despite its partly controversial history, the Fe-Cu system has emerged as an interesting prototype system for surface magnetism and also triggered a plethora of theoretical investigations.⁴⁵⁻⁵⁰

For films grown at room temperature, the structure and magnetic moment of the Fe film as a function of film thickness can be divided into three ranges:^{2,11,35} in range I, films below 4 ML Fe grow as strained bcc(110) lattice with a nanomartensitic structure; above about 2 ML they are ferromagnetic with an out-of-plane easy axis.^{2,11,35,51} The upper limit of this range depends slightly on the hydrogen

coverage.⁵¹ In range II, 5–10 ML, Fe grows fcc with a so-called “magnetic live layer” at the top, exhibiting a (2×1) or $(2 \times 2)p4g$ reconstruction below room temperature.^{11,44,52-54} A few strained bcc “needles” may be found at room temperature, while most of the film is still nonmagnetic.⁵⁵ In range III, for more than ≈ 10 ML, the film grows in relaxed bcc(110) structure and is ferromagnetic with an in-plane easy axis.⁵⁶

The metastable fcc Fe film in range II, at a thickness of about 8 ML, can be transformed from fcc(100) to bcc(110) by Ar^+ ion irradiation at room temperature.⁵⁷ This transformation was investigated with scanning-tunneling microscopy (STM), low-energy electron diffraction (LEED) and surface magneto-optic Kerr effect (SMOKE) measurements. When varying the ion energy, the best results for transformation were observed for Ar^+ ions with 1 keV (Ref. 57); the low efficiency of ions with higher energy was explained by ion-induced Fe-Cu intermixing impeding the transformation. By irradiation with a prototype ion lithography system, it was also shown that this system bears the potential for creating nanoscale ferromagnetic structures without optical lithography.⁵⁷ Considering possible technical applications and to overcome the superparamagnetic limit for small structures, films thicker than 8 ML are desirable.

In the current work, we describe the ion-induced fcc-bcc transformation of thicker fcc Fe films grown by evaporating Fe at an increased CO background pressure. This technique of stabilizing fcc Fe is based on previous work by Kirilyuk *et al.*^{40,41} It was reported that up to 60 ML of fcc Fe can be grown using different gases such as CO, ethylene, acetylene, oxygen, and their combinations; CO dissociates into carbon and oxygen, contributing to the bulk and surface stability of the fcc Fe film, respectively.^{40,41} We report on such films with a thickness of about 22 ML and we present a detailed study of the ion-induced transformation of these films, including magnetic measurements by SMOKE. All experiments were conducted at RT.

II. EXPERIMENTAL SETUP AND PREPARATION

Our experiments were carried out in two different ultra-high vacuum (UHV) systems, one focusing on structural analysis and the other focusing on magnetic properties. The structural analysis UHV setup comprises two chambers, the preparation chamber and the analysis chamber. The preparation chamber, equipped with an Ar^+ ion source for sputtering, an electron-beam heating stage for annealing, electron-beam evaporators and a gas cracker for dosing atomic hydrogen, has base pressure below 10^{-10} mbar as measured with a Penning gauge. The analysis chamber contains a customized commercial STM (Omicron μ -STM) operated in constant current mode with an electrochemically etched W tip. Auger electron spectroscopy (AES) was performed with a cylindrical mirror analyzer with a concentric electron source. The chamber also includes the instrumentation for LEED, x-ray photoelectron spectroscopy (XPS), and low-energy ion scattering (LEIS) as well as a quadrupole mass spectrometer used to measure residual gas composition. The typical pressure in this chamber was below 5×10^{-11} mbar (Bayard Alpert gauge).

The other UHV setup is a single chamber consisting of almost same facilities as for the sample preparation and characterization as mentioned before except for STM and XPS. The base pressure in this chamber was below 5×10^{-11} mbar (Bayard Alpert gauge). In this system, we used a SMOKE system to measure hysteresis curves using a He-Ne laser (632.8 nm) and a photo elastic modulator.⁵⁸ The laser beam is linearly polarized at an angle of 45° with respect to the plane of incidence and modulated before it enters the vacuum chamber; the angle of incidence on the sample is 60° with respect to the surface normal. In the present paper, the polarization analyzer was set to select *p*-polarized light. The magnetic field was parallel to the surface (longitudinal SMOKE).

The Cu(100) crystal was cleaned by sputtering using 2 keV Ar^+ ions ($I_{\text{sample}} = 2 \mu\text{A}$, typically 30 min) and annealing (520°C , 10 min). A few sputtering-annealing cycles resulted in large flat Cu terraces with widths around 100 nm and a clean surface was determined by AES. Fe films were evaporated from tips of Fe rods (2 mm thick, purity 99.99 + %) heated by electron bombardment; the deposition rate of typically 1 ML/min was calibrated by placing a quartz crystal microbalance at the sample position. To suppress high-energy ions, which may modify the growth mode of the films,⁵⁹ we have applied a retarding voltage of +1.5 kV to a cylindrical electrode in the orifice of the evaporator (the so-called “flux monitor” electrode), repelling the ions, which cannot have an energy higher than that given by the voltage of the rod (1–1.2 kV). During Fe deposition, the pressure in the UHV chamber was below 1×10^{-10} mbar unless additional CO gas was dosed to prevent the fcc-to-bcc transformation of the films.

The ion source used for the fcc-bcc transformation was scanning the sample at perpendicular incidence (SMOKE setup) or at an incidence angle of 20° with respect to the sample normal (STM setup; perpendicular incidence is not possible in this chamber). The effect of the ions at these two angles of incidence should be almost identical at ion energies

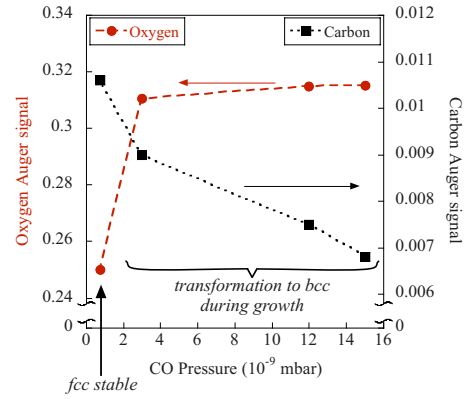


FIG. 1. (Color online) Carbon and oxygen Auger signals for 22 ML Fe films as a function of CO pressure during evaporation. Normalized Auger peak-to-peak heights of carbon $\text{C}_{273}/(\text{Fe}_{703} + \text{Cu}_{920})$ and oxygen $\text{O}_{514}/(\text{Fe}_{703} + \text{Cu}_{920})$ show an increase in oxygen and decrease in carbon concentration with increasing CO pressure.

up to 1 keV, where channeling is negligible. At higher ion energies, perpendicular incidence will lead to a somewhat higher penetration depth of the ions.⁶⁰ In the ion sources, a significant fraction of the fast Ar^+ ions gets neutralized by Ar atoms in the gas (charge transfer is a resonant process and thus has a high cross section). The neutrals are not affected by the deflection plates and electrostatic lenses, only collimated by the apertures. To achieve well-defined ion doses, we found it essential to place the sample in a position where the area used for later analysis is outside the impact area of the neutrals, i.e., outside the axis of the ion source. The time-averaged ion flux was measured with a Faraday cup, biased at +27 V to eliminate the influence of secondary electrons on the current measurement. In the STM system, where some Faraday-cup measurements were inaccurate due to secondary electrons reaching the wiring of the Faraday cup, we have also used measurements of the sample current (corrected for secondary electrons by putting the sample on positive bias) and the irradiated area. The ion flux was $\approx 10^{12} \text{ cm}^{-2} \text{ s}^{-1}$.

III. RESULTS AND DISCUSSION

A. Growth and properties of the film

As mentioned above, to stabilize the fcc structure of Fe films well above 10 ML, we have grown the films while dosing CO at a fixed background pressure.^{40,41} We found it necessary to optimize the value of the CO pressure for obtaining a stable fcc Fe film: the exact value seems to depend on details of the vacuum chamber (possibly related to the different geometries of the gas valves, pressure gauge and sample). For that purpose, we conducted experiments at different CO pressures. In one system (STM) we got the best results with 7.5×10^{-10} mbar, and in the other one (SMOKE system) we found that 3×10^{-9} mbar CO is suitable for growing a 22-ML-thick fcc Fe film.

The concentrations of oxygen and carbon in the Fe film as a function of CO pressure during evaporation are shown in Fig. 1 (data are from the STM UHV system). With increasing CO pressure, the normalized Auger peak-to-peak height

(APPH) of carbon $C_{273}/(Fe_{703}+Cu_{920})$ shows a decrease, whereas the oxygen $O_{514}/(Fe_{703}+Cu_{920})$ signal increases. In agreement with Ref. 41, this observation can be explained in the following way: the dissociation of CO takes place at the surface of the growing Fe film. Atomic carbon is incorporated in the interstitial sites of the Fe lattice, contributing to the stability of the fcc lattice in the bulk of the film. Oxygen floats on the top of the film, contributing to surface stability of the fcc lattice. This process continues until the oxygen coverage on the surface is high enough to block the adsorption and dissociation of CO molecules. If the CO pressure is too high, CO adsorption gets blocked before growth is finished, resulting in the uppermost Fe layers having very low carbon concentration, too low to sustain the fcc structure. Now, considering the same Fe evaporation rate as for the former case, if the CO pressure is too low, the concentration of carbon atoms in the interstitial sites of the Fe lattice is too low. Hence, the film will again transform to bcc before the final thickness is reached, and continue to grow in the bcc phase. Therefore, the CO pressure optimum for stabilization of the fcc film is just below the value that would lead to saturation of the surface with oxygen at the end of the growth process.

If the CO pressure is outside the range leading to a homogeneous fcc film, bcc crystallites can be observed in the 22 ML films. Figure 2 shows the surface obtained in such an experiment, where the CO pressure of 7.5×10^{-10} mbar was not stable during film growth. This instability in the CO pressure was due to slow response of the CO gas valve, a problem that was solved in the later experiments. Most of the surface is fcc and rather flat (layer-by-layer growth). The bcc areas are easily recognizable by their rough appearance and larger average height due to 5–10% larger interlayer distance of bcc Fe(110) compared to fcc Fe(100).^{55,57} They are wavy and varying in length (typically few tens of nm to 100 nm) and width (≈ 10 –20 nm). Figures 2(b)–2(d) provide higher magnification (zoom-in at the dotted area) of Fig. 2(a). The surface of the bcc area is quite rough compared to the fcc regions. Oxygen atoms are weakly visible as dark dots in Fig. 2(d), forming a $c(2 \times 2)$ lattice in the fcc areas and disordered structures in the bcc areas. In pure Fe films, the bcc structure nucleates in straight, narrow crystallites (needles) oriented along the $[011]$ and $[0\bar{1}1]$ direction; this is true for both the spontaneous and ion-induced fcc-to-bcc transformation.^{55,57} Here, we have carbon in the Fe film. We consider it likely that carbon hinders the formation of straight needles, thus the initial bcc nucleation site does not grow as a straight needle but takes a wavy path. This may be either due to a slightly inhomogeneous carbon concentration or due to carbon pileup in case that some carbon atoms diffuse out of the bcc regions into the more favorable fcc regions. Similarly, oxygen on the surface may also push the bcc needle away from straight line to wavy path. The flower-shaped bcc areas [e.g., at the right edge of Fig. 2(c)] must also be considered a consequence of carbon and/or oxygen as these shapes are not found on the clean films.

Besides the bcc needles protruding from the fcc surface, we also find areas that are lower than the fcc surroundings. Figure 2(e) shows an STM image including such an area

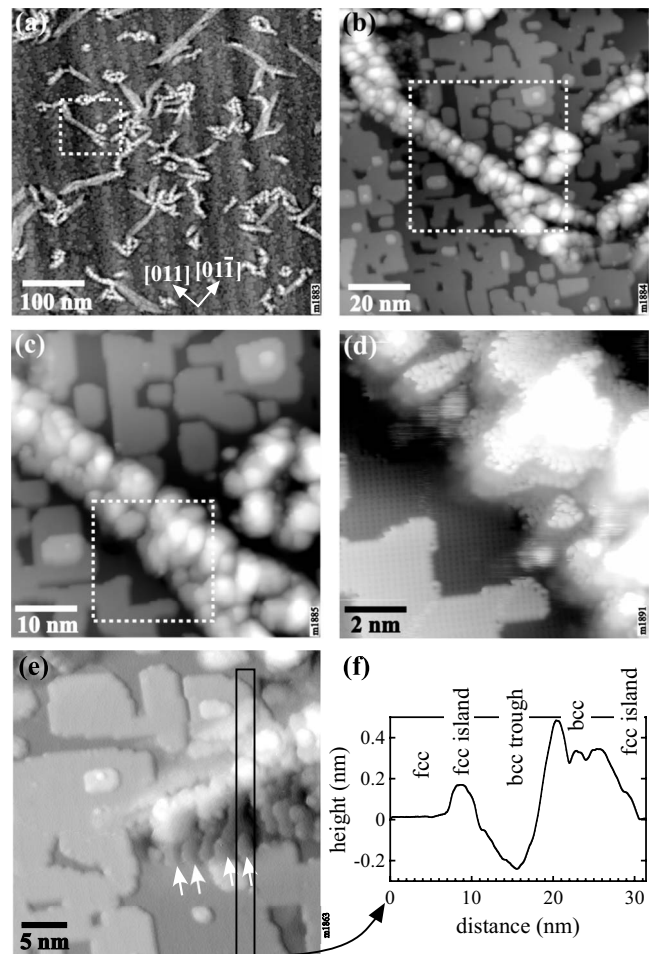


FIG. 2. STM images of a 22 ML Fe film grown with unstable CO pressure during the experiment, leading to a surface with bcc crystallites (bright). Frames (a)–(d) show the same area with increasing magnification. (e) bcc area with an adjacent trough (image shown as if illuminated from the left). The inclined bcc wedges in the trough are indicated with arrows. The section profile (f) over the vertical frame in (e) shows the bcc trough next to the needle.

(below the bright needle); a line scan across the trough and the needle (averaged over the frame) is shown in Fig. 2(f). These troughs have a typical width of ≈ 10 nm and can reach a depth of ≈ 0.5 nm below the fcc surface. They are always found at the sides of bright (high) needles and characterized by elongated wedgelike terraces perpendicular to the needle direction. These terraces are tilted by angles between 3° and 5° . This shape and tilt angle is characteristic for the Pitsch orientation of bcc crystallites as reported by Kalki.²⁹ Therefore, these troughs have to be identified as bcc areas; and we can identify similar dark areas adjacent to bright needles as bcc even in images with lower resolution.

The lower height (darker appearance) of these bcc troughs can be explained as follows: formation of a bcc needle attached to the fcc lattice at its sides is accompanied by tensile strain.^{35,55} To attain a relaxed state, the needle shrinks in width, deforming the fcc film on its sides. Obviously, the fcc film adjacent to the needle transforms to bcc due to the stress^{2,35,40,55} and due to the lateral expansion it has to reduce its height. The atomic volume increases by only 3.5% by the

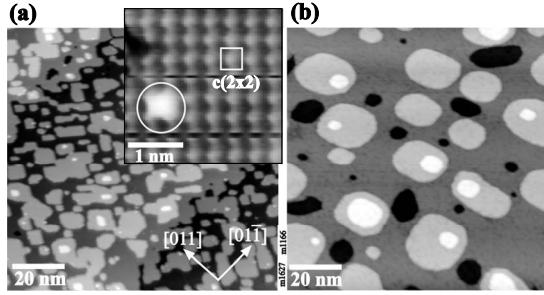


FIG. 3. STM image of the as-grown 22 ML Fe film in the presence of CO. (a) The inset shows the oxygen $c(2 \times 2)$ superstructure highlighted by a white square. The white spot in the inset is probably the missing oxygen atom (white circle). (b) The surface of an 8 ML Fe film grown without CO (shown for comparison).

fcc \rightarrow bcc transformation in the bcc regions next to the island, but the tensile strain of the needle amounts to 9% and 3% in the directions parallel and perpendicular to the needle, respectively. Thus we find an overall reduction in the height of the “trough” areas next to the needles.

The surface of a 22-ML-thick fcc Fe film grown with an optimized CO pressure is shown Fig. 3(a). We find almost perfect layer-by-layer growth; the islands show rounded rectangular shapes. This is slightly different from the surface of 8 ML films grown without CO shown in Fig. 3(b), where the islands are larger and more circular. No bcc crystallites (needles) were observed. The inset in Fig. 3(a) shows the $c(2 \times 2)$ superstructure of oxygen on fcc Fe, with the primitive superstructure cell highlighted by a white square. The white spot (marked by a circle) is probably a missing oxygen atom.

It is interesting to note that the steps of the 22 ML film grown in CO are not aligned in the close-packed $\langle 011 \rangle$ directions but rather along $\langle 010 \rangle$. This must be seen as a consequence of the $c(2 \times 2)$ oxygen overlayer, which obviously stabilizes the steps running parallel to the oxygen rows (Fig. 4).

To analyze the effect of loss of oxygen on the fcc film, we used atomic hydrogen to remove surface oxygen without ion bombardment. We prepared a slightly thicker Fe film in CO, with a thickness of 23–24 ML according to the AES (quantification was based on the average AES signals of 22 ML films and the decay of the copper signal with film thickness calculated with the SESSA code⁶¹). In the spirit of a worst-case study, the slightly larger thickness was chosen to increase the sensitivity toward any factors promoting the fcc to bcc transformation. Figure 5(a) shows the STM image of the as-grown fcc film, which is already partially transformed,

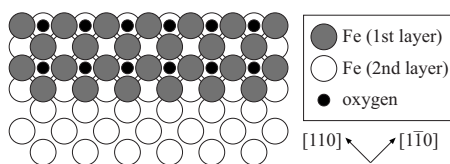


FIG. 4. Structure model for the Fe steps of the films grown in CO (top view). The $c(2 \times 2)$ oxygen superstructure is shown only in the upper layer.

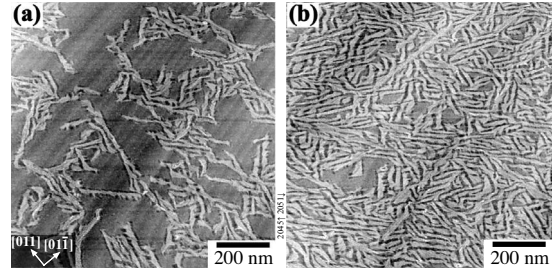


FIG. 5. Fe film (≈ 23 to 24 ML) grown in CO. (a) STM image of the as-grown surface with partially transformed areas (bright). (b) After dosing atomic hydrogen to remove the surface oxygen.

thus really at the stability limit of fcc films. This surface shows long bcc crystallites covering about 50% of the surface. The initial $O_{514}/(Fe_{703} + Cu_{920})$ APPH ratio was 0.34, roughly the same as for all the films, i.e., a closed $c(2 \times 2)$ overlayer. Oxygen was removed by exposing the surface to atomic hydrogen using a hot-tube gas cracker. We have used a pressure of 2×10^{-6} mbar H_2 for 1 h and a heating power of 55 W, which should correspond to a dose of atomic hydrogen of $> 10^{18}$ cm^{-2} . After dosing atomic H, AES shows an APPH ratio of $O_{514}/(Fe_{703} + Cu_{920})$ of 0.06, i.e., more than 80% of the initial oxygen was removed from the surface. The STM image in Fig. 5(b) shows the surface of the film after oxygen removal. The transformed area has now increased to $\approx 90\%$, but there are still some untransformed patches of ≈ 100 nm size. This transformation occurred by removal of oxygen due to adsorption of hydrogen; but we cannot exclude some influence of energetic ions created in the gas cracker and accelerated onto the surface (the hot tube is at +1 kV). As the effect of hydrogen destabilizing the fcc structure must be considered rather small (cf. Refs. 51 and 53), this experiment confirms the role of oxygen on the surface for the stability of the thick fcc Fe films, but it also allows us to compare the effect of oxygen removal with other ion-induced effects (see below).

We should finally note that a surface like that in Fig. 2 will still exhibit strong oscillations of the diffraction signals during growth, thus it would be still considered an fcc surface in medium-energy electron diffraction (MEED) experiments like those performed in Refs. 40 and 41. A surface already containing (ferromagnetic) bcc nuclei as in Fig. 2 is not useful for nanopatterning, however. This means that practical limit of the Fe thickness for such experiments is somewhere around the 22 ML thickness studied in this work, not at 30–35 ML, where the oscillations indicating growth of fcc Fe stabilized by CO die out.^{40,41}

B. Ion-induced transformation: STM and LEED

Figure 6 shows the transformation of a 22 ML fcc Fe film prepared in 7.5×10^{-10} mbar CO after bombardment with 500 eV Ar^+ ions. The as-grown film surface is stable fcc with no bcc areas over a large scan area shown in Fig. 6(a). After an Ar^+ ion dose of 1.3×10^{15} cm^{-2} , bcc nucleation areas become visible [Fig. 6(b)]. Again, the bcc regions appear brighter than the rest of the surface because of the larger interlayer distance. The bcc regions are mostly 100–200 nm

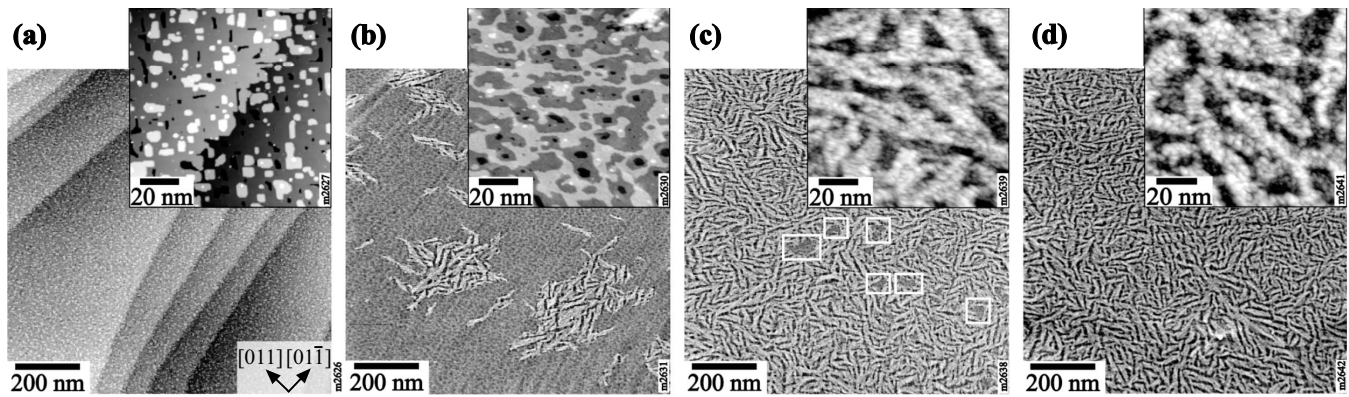


FIG. 6. Scanning tunneling microscopy images of a 22 ML Fe film prepared in 7.5×10^{-10} mbar CO. (a) as-grown film, and after 500 eV Ar^+ ion irradiation with ion doses of (b) $1.3 \times 10^{15} \text{ cm}^{-2}$, (c) $1.8 \times 10^{15} \text{ cm}^{-2}$, and (d) $2.4 \times 10^{15} \text{ cm}^{-2}$. Overview images (b)–(d) are high-pass-filtered to make the bcc needles more visible in spite of steps in the substrate.

long and 10–25 nm wide. Similar to the results for ion bombardment of clean Fe films,⁵⁷ there are only very few sites where the fcc-to-bcc transformation has nucleated, and the transformation spreads out from these sites. Zooming in on the surface shows slightly increased roughness also in the untransformed areas because the surface was sputtered [inset of Figs. 6(a) and 6(b)]. When increasing the Ar^+ ion dose to $1.8 \times 10^{15} \text{ cm}^{-2}$, most of the surface in Fig. 6(c) shows wavy bcc needles, only a few regions wider than 50–100 nm remain untransformed (white boxes). Figure 6(d) shows that with further irradiation of the film, at an ion dose of $2.4 \times 10^{15} \text{ cm}^{-2}$, the fcc to bcc transformation reaches saturation. The inset shows a zoom-in, both the bright bcc regions and the surrounding areas are quite rough. In Fig. 6(d), the fraction of the bright areas is $\approx 60\text{--}70\%$ of the film.

As already indicated by the dark bcc troughs shown in Fig. 2(e), an apparent height below that of the bcc needles does not necessarily indicate an fcc structure of the dark regions. A detailed inspection of the STM images rather shows that bcc troughs and other areas with wedgelike bcc structure extending from the bright needles are much more common in the ion-irradiated films than in the as-grown films. In irradiated films, isolated bright bcc needles are often flanked by bcc troughs, with a total trough width sometimes comparable to the width of the bright needle. At higher ion doses like in Fig. 6(c) the surface is too rough to see facets; there we can only rely on the height information to discriminate between fcc and bcc. We find that the bright needles are typically 0.3–0.4 nm higher than the fcc areas, while the areas in-between the needles are typically lower than the fcc regions, in the same height range as reported for the wedge-type bcc areas observed on unirradiated samples. Also this indicates that the areas between the bright needles are bcc.

Even at ion doses as low as in Fig. 6(b), the crystallographic structure of the bcc crystallites cannot be easily resolved by STM due to the high step density induced by sputtering. We could get sufficient resolution only on a film with preexisting bcc areas as in Fig. 2, where mild sputtering with an ion dose of $3 \times 10^{14} \text{ cm}^{-2}$ was sufficient to significantly increase the bcc area fraction. We did not obtain atomic resolution of the Fe lattice but rather see the oxygen superstructure. As shown in Fig. 7(a), the fcc Fe surface with its

$c(2 \times 2)$ overlayer and the 90° angle between the [010] and [001] directions can be seen very clearly. The structure of the bcc area in the lower left of the image is less clear because the oxygen adatoms are poorly ordered in this area. To examine the structure of the needle, we have removed drift-induced distortion of the image [taking the $c(2 \times 2)$ area as a reference] and analyzed the bcc area in the Fourier domain. We found peaks corresponding to bcc(110), obviously caused by a partial occupation of the bcc(110) lattice with oxygen atoms in equivalent sites [inset in Fig. 7(b), arrowed]. A back transform of these Fourier components shows the full bcc(110) lattice with a bond angle of $71 \pm 0.5^\circ$ [Fig. 7(b)]. This nicely agrees with the bond angle of 70.5° in bulk bcc Fe, whereas a bond angle of 75° is observed in thin (5–8 ML) films where the Fe film remains commensurate with the underlying Cu(100) substrate.^{2,55} This means that these bcc crystallites in the 22 ML Fe films have a bulklike bcc structure as expected for such a thick film.

Figure 8 shows a comparison of the surfaces of the 22 ML fcc Fe films irradiated with different ion energies (a) 500, (b) 2000, and (c) 4000 eV. These images show saturation where the transformed area does not increase with ion dose any more; the ion doses are well below twice the saturation

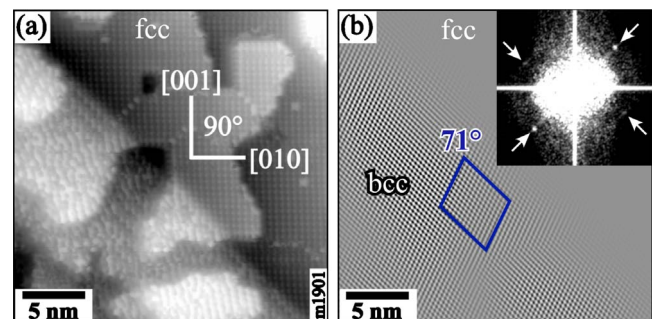


FIG. 7. (Color online) High-resolution STM image of the film in Fig. 2 after bombardment with 1 keV Ar^+ ions (dose: $3 \times 10^{14} \text{ cm}^{-2}$). (a) The bcc area in the lower left shows to poorly ordered oxygen while the well-ordered $c(2 \times 2)$ -O structure with its 90° bond angle is clearly seen in the bcc areas. (b) Filtering in the Fourier domain (spots marked in the inset) clearly shows the bcc lattice with a bond angle of $71 \pm 0.5^\circ$.

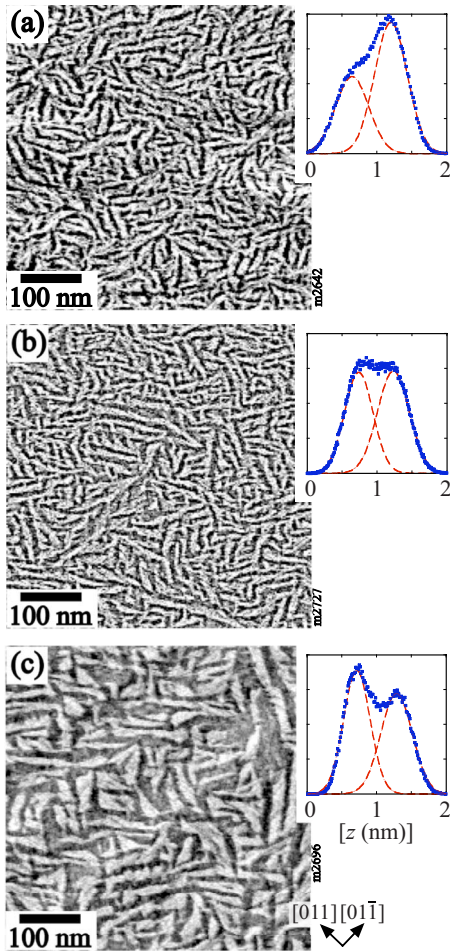


FIG. 8. (Color online) STM images of the 22 ML fcc Fe film irradiated with different Ar^+ energies: (a) 500, (b) 2000, and (c) 4000 eV. Height histograms are shown at the right.

dose, however. Due to the high ion doses needed to achieve saturation, the surface is too rough to discriminate between fcc and bcc areas by their morphology. We have high pass filtered the images to remove the underlying substrate steps and obtained height histograms. These histograms show a bimodal distribution, confirming the visual impression of bright bcc needles and darker areas. Fitting the histograms with a sum of two Gaussians, we can determine the fraction of the bright bcc needles. For the three ion energies in Fig. 8, we obtain values of 60%, 52%, and 44% clearly indicating a decrease in the bright bcc transformed area at high ion energies. Also the bright bcc regions for 500 and 2000 eV are more connected in comparison to 4000 eV. As mentioned above, the dark regions of the films irradiated with 500 eV ion energy are bcc. Assuming that the ratio between the bright and dark bcc areas is constant, the lower area fraction of bright needles observed at high ion energies would indicate some untransformed (fcc) areas.

The images in Fig. 8 also show different length scales of the bright areas. Experiments with slightly different thickness of the Fe film show that the typical size of the bright patches does not depend so much on the ion energy but is a sensitive function of the film thickness, with larger bcc patches found in thicker films.

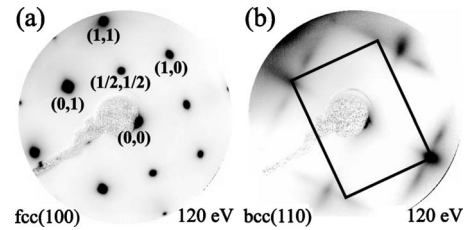


FIG. 9. (a) LEED image of the as-grown 22 ML Fe film, showing fcc(100) and oxygen $c(2 \times 2)$ spots. (b) After Ar^+ irradiation of $2.4 \times 10^{15} \text{ cm}^{-2}$ at 500 eV, diffuse bcc satellites are visible [the rectangular bcc(110) unit cell is indicated].

LEED measurements also confirm the transformation of the CO-grown 22 ML Fe film with Ar^+ ion irradiation. Figure 9(a) shows the LEED image at 120 eV of the as-grown film with fcc(100) spots indicated. The spots at $(\frac{1}{2}, \frac{1}{2})$ are caused by the $c(2 \times 2)$ oxygen superstructure. Except for the superstructure spots, this LEED pattern is the same as for 8 ML Fe films grown without CO. After Ar^+ ion irradiation at 500 eV with $2.4 \times 10^{15} \text{ cm}^{-2}$, the pattern becomes blurred and bcc(110) spots appear [Fig. 9(b)]. One out of four bcc domains is indicated by a rectangle in Fig. 9(b); the others are obtained by 90° rotation and mirroring along the fcc (1,0) or (0,1) direction. The bcc LEED spots are strongly elongated, with the spots close to the positions of the former fcc (0,1) spots blurred mainly in the radial direction and the other two spots [upper and lower corner of the rectangle in Fig. 9(b)] being elongated in a parallel direction. We attribute this elongation to the tilting of the bcc areas mentioned previously; not only the low-lying areas next to the bcc needles but also the needle surfaces themselves are often tilted in a direction that would explain this kind of blurring. The blurring perpendicular to the direction of elongation is probably due to the increased roughness of the sputtered surface.

C. Ion-induced transformation: SMOKE measurements

We have used our surface magneto-optic Kerr effect setup to study the magnetic properties of the 22-ML-thick Fe films grown in CO on Cu(100). Within the CO pressure range leading to fcc growth, the as-grown films are found to be paramagnetic at RT (curve labeled “0” in Fig. 10). The films undergo a transformation from paramagnetic to ferromagnetic when irradiated with Ar^+ ions.

Figure 10 shows the longitudinal Kerr ellipticity as a function of applied magnetic field for the 22 ML fcc Fe film bombarded with 2 keV Ar^+ ions. After a fluence of $3 \times 10^{14} \text{ cm}^{-2}$, the magnetic behavior of the film changes to ferromagnetism with an in-plane easy axis. With increasing fluence, the Kerr signal and, hence, the magnetization increases and reaches a maximum at a fluence of $6 \times 10^{14} \text{ cm}^{-2}$.

Figure 11(a) shows the longitudinal Kerr ellipticity at magnetic saturation ϵ_{sat} as a function of Ar^+ ion dose for different ion energies. For ion energies up to 2 keV, the transformation gets faster with increasing ion energy, i.e., the ions become more efficient in transforming the film to the bcc phase. For 4 keV Ar^+ ion energy, the transformation is

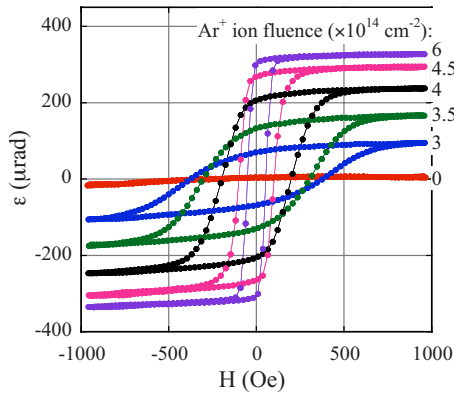


FIG. 10. (Color online) Hysteresis loops of the 22-ML Fe films irradiated with 2 keV Ar^+ ions, showing longitudinal Kerr ellipticity ε as a function of magnetic field H . The transformation from paramagnetic (ion dose: 0) to ferromagnetic with increasing ion fluence can be seen.

slower than for 2 keV and the maximum magnetization reached is lower than for lower ion energies. A similar behavior was already observed for pure 8 ML Fe films,⁵⁷ but with a decrease in the saturation magnetization at much lower ion energies (highest efficiency at 1 keV). In all curves, there is a slight decrease in the magnetization after reaching the saturation value, which is attributed to the sputter removal of Fe after prolonged irradiation with Ar^+ ions.

The maximum saturation value of the longitudinal Kerr ellipticity ε is 320 μrad , which is higher than for the pure 8 ML Fe film, where a maximum value of 150 μrad at 1 keV Ar^+ ion energy was found.⁵⁷ For a completely transformed 22 ML film we might expect the maximum saturation value to be roughly 22/8 times the value for 8 ML film, i.e., 412 μrad . This calculation ignores the decay of the light's electric field with increased film thickness, however. The optical skin depth is about 24 nm, only six times the thickness of the film, which would yield a decrease in the Kerr angle to ≈ 350 μrad at perpendicular incidence. As we are measuring at a more grazing incidence (60°), we attribute the lower value found to a faster decay with thickness at this angle.

Figure 11(b) shows the coercive field H_c as a function of Ar^+ ion dose. The coercivity is high in the beginning of ion irradiation for all energies and sharply drops with increasing ion dose. As in Ref. 54, we can explain this by separate

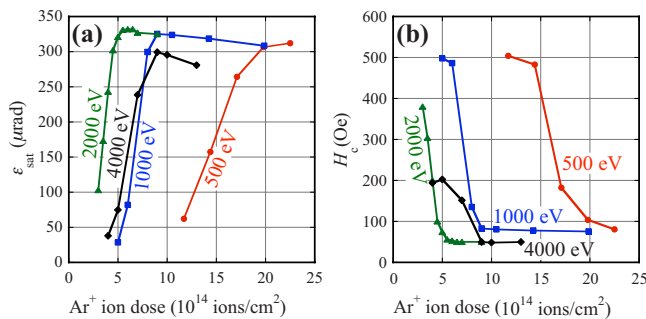


FIG. 11. (Color online) (a) Saturation value of longitudinal Kerr ellipticity ε_{sat} as a function of Ar^+ ion dose for different ion energies and (b) coercive field H_c as a function of Ar^+ ion dose.

(magnetically decoupled) needles with a large length-to-width ratio in the early stages of transformation [see Fig. 6(b)]. These needles have a high shape anisotropy and possibly also some magnetocrystalline anisotropy due to residual strain. The initial anisotropy is similar for 500 eV to 2 keV ion energy, but clearly lower for 4 keV, where the transformation is also less efficient.

D. Mechanism of the ion-induced transformation

When discussing the mechanism of the ion-induced transformation, we should first analyze whether mere removal of oxygen from the surface by sputtering could cause the transformation. We have shown that removal of more than 80% of the adsorbed oxygen is required for a transformation of much of the surface, but still leaves a few untransformed patches [Fig. 5(b)], similar to transformation by ion bombardment before saturation is reached [Fig. 6(c)]. At this stage of ion bombardment, the APPH $\text{O}_{514}/(\text{Fe}_{703}+\text{Cu}_{920})$ ratio has decreased to 72% of its initial value, i.e., less than 30% of the oxygen has been removed. Thus, the removal of oxygen by sputtering is insufficient to explain the ion-induced fcc-bcc transformation.

In Ref. 57, we have already suggested a transformation mechanism based on the so-called thermal spike model^{62,63} in sputtering. “Thermal spike” means that impact of a single ion strongly heats the target material in a small volume, and, thus, melts it. While the thermal spike model does not explain sputtering of metals by Ar^+ ions in the energy range under consideration (sputtering is caused by the collision cascade),⁶⁴ the existence of a molten volume after an ion impact is established by computer simulations as well as by the outflow of material from that volume.^{65,66} A few picoseconds after the impact, the material is quickly cooled by heat exchange to the surrounding regions and crystallizes. Usually, crystallization will be pseudomorphic to the surrounding lattice, but it is easily conceivable that various crystallographic defects can be created by rapid quenching of the molten volume. Especially in case of a collision cascade with two or more hot spots (created by fast recoils), the resolidification front will be nonspherical and it may happen that crystallization from two opposite sides results in a sheared structure, which may form the nucleus of a bcc crystallite [Fig. 12(b)]. Creation of a stable bcc nucleus must be a rather rare process, as evidenced by the low number of nuclei observed in the STM images [$\approx 3 \times 10^{-5}$ nm^{-2} in Fig. 6(b), i.e., $\approx 2 \times 10^{-6}$ per impinging ion]. As soon as a bcc crystallite has formed, it may grow by further ion impacts, either through recrystallization from the melt or by defects that make it possible to shear a larger area into its stable bcc arrangement (cf. Refs. 2 and 55).

For a better idea about the numbers involved, we have employed binary collision cascade simulations with the SRIM code⁶⁷ to calculate the energy transferred to the target, E_{nuc} . According to Ref. 68, the number of atoms N_m in the melt can be estimated as $N_m \approx 0.07 E_{\text{nuc}} / (k_B T_m)$, where k_B is the Boltzmann constant and T_m is the melting temperature. With increasing Ar^+ ion energy, the number of atoms in the melt increases, but above an energy of approximately 2 keV the

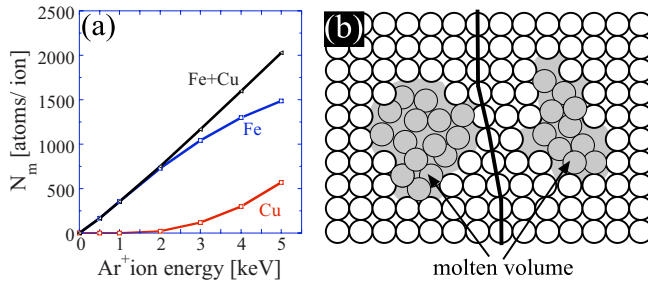


FIG. 12. (Color online) (a) Calculated number of atoms N_m in the molten volume for a 22-ML-thick fcc Fe film. The fraction of Cu atoms in the melt is negligible up to 2 keV and increases with increasing ion energy. (b) Schematic view of an arrangement leading to a sheared structure during recrystallization, a possible bcc nucleus.

collision cascade also reaches the Cu substrate and intermixing between Fe and Cu occurs, as shown in Fig. 12(a). With Cu favoring the fcc structure, mixing will be detrimental for the fcc-bcc transformation. This result nicely explains the reduced transformation efficiency at an ion energy of 4 keV, leading to a lower bcc fraction after the transformation, seen in both STM (Fig. 8) and the magnetization data [Fig. 11(a)]. Intermixing might also explain the lower coercivity of the films transformed by 4 keV Ar^+ [Fig. 11(b)]. The importance of intermixing is supported by comparison with the data for 8 ML films in Ref. 57, where the maximum efficiency of the transformation was observed at 1 keV, again just before the collision cascade reaches the substrate and intermixing can occur.

E. 22 ML Fe films covered by Pd and Au

For any technological applications, the films must be covered with a protective layer to prevent oxidation. Oxidation resistance is also needed when transferring the Fe-coated Cu crystal in ambient conditions to a focused ion beam facility. We have therefore covered the 22 ML fcc Fe film prepared in CO with two metals, Pd and Au. In contrast to pure iron films, we have to examine whether oxygen at the surface of the Fe films prevents wetting by the overlayer material. It is also interesting to see whether the fcc-bcc transformation can be still detected by STM after coating.

Figure 13 shows the 22 ML fcc Fe film prepared in CO and covered with 2.25 nm Pd [this corresponds to 10 ML Pd(111) or 10 ML of a hypothetical pseudomorphic overlayer on Cu(100)]. The STM images [(a) and (b)] show a continuous film, i.e., no dewetting, but no layer-by-layer growth. Although the images are not perfect and also distorted, we clearly see that part of the film shows a Pd(100) surface, while other areas are predominantly Pd(111); some crystallites have a size of only a few nm. It is likely that grain-boundary diffusion of oxygen will occur through the Pd film, thus we do not consider Pd a good protective overlayer.

Figure 14(a) shows an STM image of the as-prepared surface of the 22 ML fcc Fe film. It is then covered by 0.52 and 2 nm gold [corresponding to 2.2 and 8.5 ML Au(111), re-

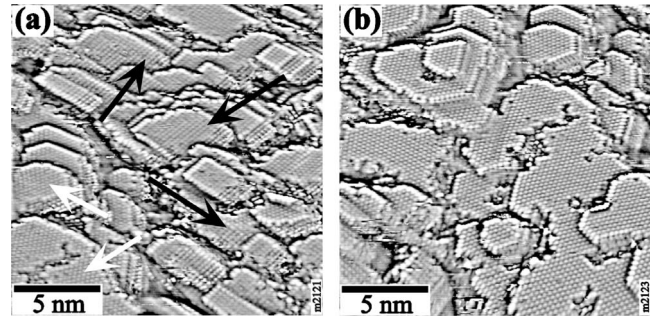


FIG. 13. STM images (strongly high-pass filtered) of the 22 ML fcc Fe film covered with 2.25 nm Pd. (a) Pd grows in (100) orientation in the regions indicated with black arrows and as (111) indicated with white arrows. (b) Most of this area shows (111) growth.

spectively]. Figure 14(c) shows almost perfect layer-by-layer growth, and also the 2-nm Au film exhibits good layer-by-layer growth. The lattice matching between bcc Fe(110) and Au(111) is much better than that between fcc Fe(100) and Au(111), therefore, we have suggested previously that a Au overlayer could facilitate the fcc-bcc transformation.⁵⁷ We have therefore grown a film on the verge of the fcc-bcc transformation to check for any Au-induced transformation [compare Figs. 14(a) and 14(b)]. We found only a small increase in the bcc area fraction by Au deposition.

This gold-coated film was then transformed to bcc by 3 keV Ar^+ ion irradiation. Figure 14(d) shows that most of the film was transformed with an ion dose of $9 \times 10^{14} \text{ cm}^{-2}$; we cannot detect any untransformed areas. We should mention here that the ion energy of 3 keV would be sufficient for some Fe-Cu intermixing in the uncoated film. For the film

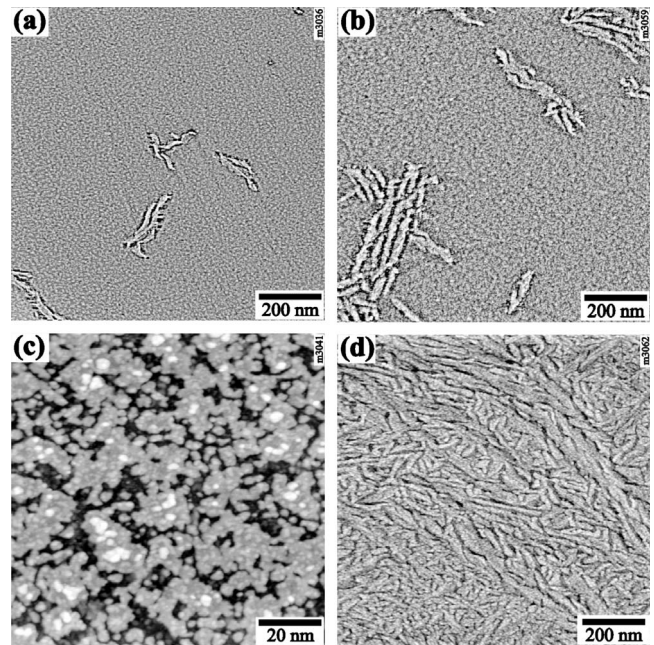


FIG. 14. STM images of the 22 ML fcc Fe film (a) as prepared in 7.5×10^{-10} mbar CO pressure and after deposition of (c) 0.52 nm and (b) 2 nm Au. (d) Surface covered with 2 nm Au after irradiation with $9 \times 10^{14} \text{ cm}^{-2} Ar^+$ ions at 3 keV.

coated with 2 nm Au, the Fe-Cu interface is out of reach for the ions. Thus, no Fe-Cu intermixing will impede the fcc-bcc transformation. On the other hand, lower energies as preferred for the uncoated films would be insufficient to penetrate the Au capping layer. It is interesting to note that Au-Fe intermixing, though certainly occurring, seems to have no negative influence on the transformation.

IV. SUMMARY

We have successfully stabilized 22-ML-thick fcc Fe films on Cu(100) at RT by growing with suitable CO background pressures. AES data suggest that carbon and oxygen are responsible for the bulk and surface stability of the film, respectively. STM images show layer-by-layer growth; STM and LEED also confirmed the fcc(100) structure of these films.

After bombarding the surface with Ar⁺ ions, the film transforms from fcc to bcc. Needlelike bcc crystallites are easily recognized in the STM images, slightly higher than fcc surface; in addition, areas next to the needles, but lower than the fcc areas are also bcc. The transformation was confirmed by the appearance of bcc spots in the LEED image.

SMOKE measurements showed that the structural transformation is accompanied by a magnetic transformation from paramagnetic (fcc Fe) to ferromagnetic (bcc Fe). Coercivity decreased rapidly with Ar⁺ ion fluences for all Ar⁺ ion energies. The transformation rate was found to depend on the Ar⁺ ion energy; the fastest transformation was observed for 2 keV Ar⁺. At higher energies, Fe-Cu intermixing at the interface impedes the transformation. Nucleation of the bcc phase occurs only in a very low fraction of all ion impacts. We have proposed that the process responsible for bcc nucleation is recrystallization of the small volume molten by ion impact (thermal spike).

We also showed that these films could be coated with Pd and Au; Au grows in an almost layer-by-layer fashion and possibly causes the fcc-bcc transformation of a small fraction of a film already on the verge of the transformation. The ion-induced transformation is possible by bombarding the Au-coated film.

ACKNOWLEDGMENTS

This work was financially supported by the Austrian *Fonds zur Förderung der wissenschaftlichen Forschung* and the Higher Education Commission of Pakistan.

-
- ¹M. Wuttig and X. Liu, *Ultrathin Metal Films: Magnetic and Structural Properties* (Springer, New York, 2004).
- ²A. Biedermann, R. Tscheliessnig, M. Schmid, and P. Varga, *Appl. Phys. A: Mater. Sci. Process.* **78**, 807 (2004).
- ³W. A. Jesser and J. W. Matthews, *Philos. Mag.* **15**, 1097 (1967).
- ⁴M. T. Kief and W. F. Egelhoff, Jr., *Phys. Rev. B* **47**, 10785 (1993).
- ⁵D. P. Pappas, K. P. Kämper, and H. Hopster, *Phys. Rev. Lett.* **64**, 3179 (1990).
- ⁶C. Liu, E. R. Moog, and S. D. Bader, *Phys. Rev. Lett.* **60**, 2422 (1988).
- ⁷W. A. A. Macedo and W. Keune, *Phys. Rev. Lett.* **61**, 475 (1988).
- ⁸D. A. Steigerwald and W. F. Egelhoff, Jr., *Phys. Rev. Lett.* **60**, 2558 (1988).
- ⁹D. P. Pappas, K. P. Kämper, B. P. Miller, H. Hopster, D. E. Fowler, A. C. Luntz, C. R. Brundle, and Z. X. Shen, *J. Appl. Phys.* **69**, 5209 (1991).
- ¹⁰F. Petroff, A. Barthelemy, D. H. Mosca, D. K. Lottis, A. Fert, P. A. Schroeder, W. P. Pratt, Jr., R. Loloee, and S. Lequien, *Phys. Rev. B* **44**, 5355 (1991).
- ¹¹J. Thomassen, F. May, B. Feldmann, M. Wuttig, and H. Ibach, *Phys. Rev. Lett.* **69**, 3831 (1992).
- ¹²P. Xhonneux and E. Courtens, *Phys. Rev. B* **46**, 556 (1992).
- ¹³R. Allenspach and A. Bischof, *Phys. Rev. Lett.* **69**, 3385 (1992).
- ¹⁴M. T. Kief and W. F. Egelhoff, Jr., *J. Appl. Phys.* **73**, 6195 (1993).
- ¹⁵T. Kraft, P. M. Marcus, and M. Scheffler, *Phys. Rev. B* **49**, 11511 (1994).
- ¹⁶D. Li, M. Freitag, J. Pearson, Z. Q. Qiu, and S. D. Bader, *J. Appl. Phys.* **76**, 6425 (1994).
- ¹⁷D. Li, M. Freitag, J. Pearson, Z. Q. Qiu, and S. D. Bader, *Phys. Rev. Lett.* **72**, 3112 (1994).
- ¹⁸J. Shen, H. Jenniches, C. V. Mohan, J. Barthel, M. Klaua, P. Ohresser, and J. Kirschner, *Europhys. Lett.* **43**, 349 (1998).
- ¹⁹H. Jenniches, J. Shen, C. V. Mohan, S. S. Manoharan, J. Barthel, P. Ohresser, M. Klaua, and J. Kirschner, *Phys. Rev. B* **59**, 1196 (1999).
- ²⁰D. Schmitz, C. Charton, A. Scholl, C. Carbone, and W. Eberhardt, *Phys. Rev. B* **59**, 4327 (1999).
- ²¹K. Amemiya, S. Kitagawa, D. Matsumura, H. Abe, T. Ohta, and T. Yokoyama, *Appl. Phys. Lett.* **84**, 936 (2004).
- ²²H. Magnan, D. Chandresris, B. Villette, O. Heckmann, and J. Lecante, *Phys. Rev. Lett.* **67**, 859 (1991).
- ²³D. Qian, X. F. Jin, J. Barthel, M. Klaua, and J. Kirschner, *Phys. Rev. Lett.* **87**, 227204 (2001).
- ²⁴D. A. Steigerwald, I. Jacob, and W. F. Egelhoff, Jr., *Surf. Sci.* **202**, 472 (1988).
- ²⁵M. Onellion, M. A. Thompson, J. L. Erskine, C. B. Duke, and A. Paton, *Surf. Sci.* **179**, 219 (1987).
- ²⁶W. Daum, C. Stuhlmann, and H. Ibach, *Phys. Rev. Lett.* **60**, 2741 (1988).
- ²⁷P. Bayer, S. Müller, P. Schmailzl, and K. Heinz, *Phys. Rev. B* **48**, 17611 (1993).
- ²⁸K. E. Johnson, D. D. Chambliss, R. J. Wilson, and S. Chiang, *J. Vac. Sci. Technol. A* **11**, 1654 (1993).
- ²⁹K. Kalki, D. D. Chambliss, K. E. Johnson, R. J. Wilson, and S. Chiang, *Phys. Rev. B* **48**, 18344 (1993).
- ³⁰M. Wuttig and J. Thomassen, *Surf. Sci.* **282**, 237 (1993).
- ³¹P. Schmailzl, K. Schmidt, P. Bayer, R. Döll, and K. Heinz, *Surf. Sci.* **312**, 73 (1994).
- ³²H. Zillgen, B. Feldmann, and M. Wuttig, *Surf. Sci.* **321**, 32

- (1994).
- ³³S. Müller, P. Bayer, C. Reischl, K. Heinz, B. Feldmann, H. Zillgen, and M. Wuttig, *Phys. Rev. Lett.* **74**, 765 (1995).
- ³⁴M. Straub, R. Vollmer, and J. Kirschner, *Phys. Rev. Lett.* **77**, 743 (1996).
- ³⁵A. Biedermann, R. Tscheliessnig, M. Schmid, and P. Varga, *Phys. Rev. Lett.* **87**, 086103 (2001).
- ³⁶D. D. Chambliss, R. J. Wilson, and S. Chiang, *J. Vac. Sci. Technol. A* **10**, 1993 (1992).
- ³⁷J. Giergiel, J. Shen, J. Woltersdorf, A. Kirilyuk, and J. Kirschner, *Phys. Rev. B* **52**, 8528 (1995).
- ³⁸H. L. Meyerheim, R. Popescu, D. Sander, J. Kirschner, O. Robach, and S. Ferrer, *Phys. Rev. B* **71**, 035409 (2005).
- ³⁹H. Landskron, G. Schmidt, K. Heinz, K. Müller, C. Stuhlmann, U. Beckers, M. Wuttig, and H. Ibach, *Surf. Sci.* **256**, 115 (1991).
- ⁴⁰A. Kirilyuk, J. Giergiel, J. Shen, and J. Kirschner, *Phys. Rev. B* **52**, R11672 (1995).
- ⁴¹A. Kirilyuk, J. Giergiel, J. Shen, M. Straub, and J. Kirschner, *Phys. Rev. B* **54**, 1050 (1996).
- ⁴²R. Halbauer and U. Gonser, *J. Magn. Magn. Mater.* **35**, 55 (1983).
- ⁴³D. Pescia, M. Stampanoni, G. L. Bona, A. Vaterlaus, R. F. Willis, and F. Meier, *Phys. Rev. Lett.* **58**, 2126 (1987).
- ⁴⁴A. Biedermann, R. Tscheliessnig, C. Klein, M. Schmid, and P. Varga, *Surf. Sci.* **563**, 110 (2004).
- ⁴⁵M. F. Onellion, C. L. Fu, M. A. Thompson, J. L. Erskine, and A. J. Freeman, *Phys. Rev. B* **33**, 7322 (1986).
- ⁴⁶D. D. Chambliss and K. E. Johnson, *Phys. Rev. B* **50**, 5012 (1994).
- ⁴⁷T. Asada and S. Blügel, *Phys. Rev. Lett.* **79**, 507 (1997).
- ⁴⁸R. E. Camley and D. Li, *Phys. Rev. Lett.* **84**, 4709 (2000).
- ⁴⁹S. S. A. Raze, J. B. Staunton, L. Szunyogh, and B. L. Gyorffy, *Phys. Rev. Lett.* **88**, 147201 (2002).
- ⁵⁰D. Spišák and J. Hafner, *Phys. Rev. Lett.* **88**, 056101 (2002).
- ⁵¹A. Biedermann, *Phys. Rev. B* **80**, 235403 (2009).
- ⁵²G. Rauchbauer, A. Buchsbaum, H. Schiechl, P. Varga, M. Schmid, and A. Biedermann, *Surf. Sci.* **602**, 1589 (2008).
- ⁵³C. Egawa, E. M. McCash, and R. F. Willis, *Surf. Sci.* **215**, L271 (1989).
- ⁵⁴S. Müller, P. Bayer, A. Kinne, P. Schmailzl, and K. Heinz, *Surf. Sci.* **322**, 21 (1995).
- ⁵⁵A. Biedermann, M. Schmid, and P. Varga, *Phys. Rev. Lett.* **86**, 464 (2001).
- ⁵⁶T. Detzel, N. Memmel, and T. Fauster, *Surf. Sci.* **293**, 227 (1993).
- ⁵⁷W. Rupp, A. Biedermann, B. Kamenik, R. Ritter, C. Klein, E. Platzgummer, M. Schmid, and P. Varga, *Appl. Phys. Lett.* **93**, 063102 (2008).
- ⁵⁸J. Badoz, M. Billardon, J. C. Canit, and M. F. Russel, *J. Opt.* **8**, 373 (1977).
- ⁵⁹C. Nagl, O. Haller, E. Platzgummer, M. Schmid, and P. Varga, *Surf. Sci.* **321**, 237 (1994).
- ⁶⁰D. Onderdelinden, *Appl. Phys. Lett.* **8**, 189 (1966).
- ⁶¹W. Smekal, W. S. M. Werner, and C. J. Powell, *Surf. Interface Anal.* **37**, 1059 (2005).
- ⁶²P. Sigmund, *Appl. Phys. Lett.* **25**, 169 (1974).
- ⁶³P. Sigmund, *J. Appl. Phys.* **52**, 990 (1981).
- ⁶⁴H. H. Andersen, in *Fundamental Processes in Sputtering of Atoms and Molecules (SPUT 92)*, edited by P. Sigmund (Det Kongelige Danske Videnskabernes Selskab, Copenhagen, 1993), p. 127.
- ⁶⁵M. Ghaly and R. S. Averback, *Phys. Rev. Lett.* **72**, 364 (1994).
- ⁶⁶C. Busse, H. Hansen, U. Linke, and T. Michely, *Phys. Rev. Lett.* **85**, 326 (2000).
- ⁶⁷J. Ziegler and J. Biersack, SRIM-2006 (<http://www.srim.org>).
- ⁶⁸W. Schilling and H. Ullmaier, in *Materials Science and Technology*, edited by R. W. Cahn, P. Haasen, and E. J. Kramer (Chemie, Weinheim, 1994) Vol. 10B, p. 179.